RSC Advances

PAPER

View Article Online
View Journal | View Issue

Check for updates

Cite this: *RSC Adv.*, 2023, **13**, 8564

Interfacial construction of P25/Bi_2WO_6 composites for selective CO_2 photoreduction to CO in gas–solid reactions†

Daohan Liu,[ab] Minli Zeng,[a] Zhen Li,[a] Zhiqi Zhu,[a] Yu Chen,[c] Kunyapat Thummavichai,[bc] Oluwafunmilola Ola,[d] Nannan Wang *[ab] and Yanqiu Zhu *[ab]

Received 19th January 2023
Accepted 23rd February 2023

DOI: 10.1039/d3ra00418j

rsc.li/rsc-advances

Photocatalysis provides an attractive approach to convert CO_2 into valuable fuels, which relies on a well-designed photocatalyst with good selectivity and high CO_2 reduction ability. Herein, a series of P25/Bi_2WO_6 nanocomposites were synthesized by a simple one-step *in situ* hydrothermal method. The formation of a heterojunction between Bi_2WO_6, which absorbs visible light, and P25, which absorbs ultraviolet light, expands the utilization of sunlight by the catalysts, and consequently, leads to a remarkably enhanced CO_2 selective photoreduction to CO. The maximum CO yield of the P25/Bi_2WO_6 heterojunction under simulated solar irradiation was 15.815 $\mu mol\ g^{-1}\ h^{-1}$, which was 4.04 and 2.80 times higher than that of pure P25 and Bi_2WO_6, respectively. Our investigations verified a Z-scheme charge migration mechanism based on various characterization techniques between P25 and Bi_2WO_6. Furthermore, *in situ* DRIFTS uncovered the related reaction intermediates and CO_2 photoreduction mechanism. Our work sheds light on investigating the efficacious construction of Bi_2WO_6-based hybrids for light-driven photocatalysis.

1 Introduction

The continuous consumption of global fossil energy and the increasing concentration of the greenhouse gas carbon dioxide (CO_2) has led to a severe energy crisis and environmental pollution problems, which are not in line with the requirements of sustainable human development.[1–3] Therefore, how to convert CO_2 into chemical fuels has become a pressing problem.[4,5] So far, CO_2 reduction has usually been achieved by hydrogenation reactions at high temperature and pressure or in the presence of precious metal co-catalysts.[6,7] On the other hand, inspired by plant photosynthesis, using solar energy to convert CO_2 into useable chemicals is a low-cost and environmentally friendly strategy.[8–10] Various photocatalysts, such as titanium dioxide (TiO_2), cuprous oxide (Cu_2O), carbon nitride (g-C_3N_4), strontium titanate ($SrTiO_3$), bismuth chloride (BiOCl), and tungsten oxide (WO_3), have been extensively studied and applied in this field of photocatalytic CO_2 reduction.[11–16] In general, the process of photocatalytic CO_2 consists of the following steps. First, electron–hole pairs are excited by photons, where the photon energy is equal to or greater than the semiconductor bandgap. Second, light-induced carriers are separated and transported to the surface of the photocatalyst. Third, light-induced electrons react with CO_2 at the surface-active center of the photocatalyst.[17] However, the efficiency of most single-component photocatalysts for photocatalytic CO_2 reduction is still far from practical due to the rapid compounding of electron–hole pairs and the lack of surface-active centers. In order to improve photocatalytic efficiency, one of the most effective ways is to construct heterojunction by compounding two semiconductors.[18,19] This method can improve the separation and transfer of electron–hole pairs and provide more surface-active centers for photocatalytic reactions. Therefore, the construction of suitable heterojunction is essential to improve the CO_2 reduction performance of photocatalysts.

TiO_2 has the advantages of strong redox performance, non-toxic, low price, and high stability, and it has a broad development prospect in the field of photocatalytic CO_2 reduction.[20–22] Commercial TiO_2 (P25) is a mixture of anatase and rutile TiO_2 with forbidden bandwidths of 3.2 and 3.0 eV, respectively, and a wide band gap, which has solid photocatalytic properties under UV-vis light, and its particle size ranges from 20 to 40 nm, which has a large specific surface area.[23] However, only 4% of sunlight is in the UV, and the lower light utilization and rapid

---

[a] *State Key Laboratory of Featured Metal Materials and Life-cycle Safety for Composite Structures, School of Resources, Environment and Materials, Guangxi University, Nanning, 530004, China. E-mail: wangnannan@gxu.edu.cn*

[b] *College of Engineering, Mathematics and Physical Sciences, University of Exeter, Exeter, EX4 4QF, UK. E-mail: Y.zhu@exeter.ac.uk*

[c] *Department of Mathematics, Physics and Electrical Engineering, Faculty of Engineering and Environment, Northumbria University, NE1 8ST, UK*

[d] *Advanced Materials Group, Faculty of Engineering, The University of Nottingham, Nottingham, NG7 2RD, UK*

† Electronic supplementary information (ESI) available. See DOI: **https://doi.org/10.1039/d3ra00418j**

compounding of electron–hole pairs limit the practical application of TiO_2 photocatalytic CO_2 reduction.[24,25] Therefore, several methods have been used to improve the photocatalytic performance of TiO_2, including doping, noble metal deposition, surface modification, and construction of heterojunction.[26–29] As a representative method, combining UV-responsive semiconductor TiO_2 and visible-light-responsive semiconductor to construct heterojunction facilitates carrier migration and separation. It improves the light adsorption capacity, improving its photocatalytic CO_2 reduction performance.

Bismuth tungstate (Bi_2WO_6) is a visible light-responsive bismuth-based photocatalyst with a forbidden bandwidth of about 2.8 eV, one of the Aurivillius phase oxides, it is a complex, layered material consisting of alternating stacks of $[Bi_2O_2]^{2+}$ layers and $[WO_4]^{2-}$ layers.[30] This layered structure facilitates the separation of electron–hole pairs and confers them to a high photocatalytic activity.[31] However, Bi_2WO_6 exhibited poor light absorption performance and low photoconversion efficiency at wavelengths less than 450 nm.[32] Combining Bi_2WO_6 and other semiconductor materials to construct heterojunction should be an effective strategy to solve this problem. So far, heterojunction structures have attracted significant attention in photocatalysis, and many heterojunction photocatalysts have been developed, such as Bi_2WO_6/MoO_3, $BiSn_2O_7/Bi_2WO_6$, black phosphorus/Bi_2WO_6, and g-C_3N_4/Bi_2WO_6, *etc.*[33–36] Combining P25 nanoparticles with Bi_2WO_6 can improve the photocatalytic performance. The synergistic effect between them can improve the light adsorption ability and facilitate the separation of electron–hole pairs. More importantly, the agglomeration phenomenon of P25 nanoparticles can be effectively improved. To the best of our knowledge, the application of P25/Bi_2WO_6 nanocomposites in photocatalytic CO_2 reduction has been little studied.

In this work, we have successfully prepared P25/Bi_2WO_6 nanocomposites using a simple one-step *in situ* hydrothermal method. It was used for the photocatalytic reduction of CO_2 in the absence of sacrificial agents, and the physical and photochemical properties of the material were characterized by various characterization tools. The reaction process and mechanism of the photocatalytic system were further investigated by *in situ* infrared testing. Compared with pure P25 and Bi_2WO_6, there is a strong synergy between the nanocomposites, which not only broadens the light absorption range but also suppresses the electron–hole pair recombination and has a high selectivity for carbon monoxide (CO). This study can provide new ideas for Bi_2WO_6-based nanocomposites in photocatalysis.

2 Experimental section

2.1. Materials

Sodium tungstate dihydrate ($Na_2WO_4\cdot 2H_2O$, 99.5%) and titanium dioxide (P25) were purchased from Shanghai Macklin Biochemical Co., Ltd, China. Bismuth(III) nitrate pentahydrate ($Bi(NO_3)_3\cdot 5H_2O$, 99.0%) was purchased from Sinopharm Chemical Reagent Co., Ltd, China. Cetyltrimethylammonium bromide (CTAB, 99.0%) was purchased from Damao Chemical Reagent Factory Co., Ltd, China. Sodium hydrogen carbonate ($NaHCO_3$, 99.5%) was purchased from Guangdong Guanghua Sci-Tech Co., Ltd, China. All chemicals were used as received without further purification. The water used throughout the research is deionized water.

2.2. Synthesis

2.2.1 Preparation of the P25/Bi_2WO_6 photocatalyst. P25/Bi_2WO_6 photocatalyst was prepared according to the previous reports with some modifications.[37] In a typical procedure (Scheme 1), 2 mmol $Bi(NO_3)_3\cdot 5H_2O$ and a known mass of P25 were mixed in 40 mL deionized water, which was labeled as Solution A. 1 mmol $Na_2WO_4\cdot 2H_2O$ and 0.05 g CTAB were added to 40 mL of deionized water with ultrasonic for 10 min and stirring for 30 min at ambient temperature, which was labeled as Solution B. Then Solution A was slowly added into Solution B and stirring for 30 min at ambient temperature. The resulting suspension was transferred into a 100 mL Teflon-lined autoclave and heated at 120 °C for 24 h. The final products were collected by centrifugation, washed several times with ethanol and deionized water, and dried at 60 °C in vacuum for 12 h. The mass ratios of P25 to Bi_2WO_6 were set as 10%, 20%, 30%, and 40%, and they were labeled as P25/BWO-10, P25/BWO-20, P25/BWO-30, and P25/BWO-40, respectively.

2.2.2 Preparation of Bi_2WO_6 nanosheets. For comparison, under the same experimental procedure, the pure Bi_2WO_6 were synthesized without adding P25, which was labelled as BWO.

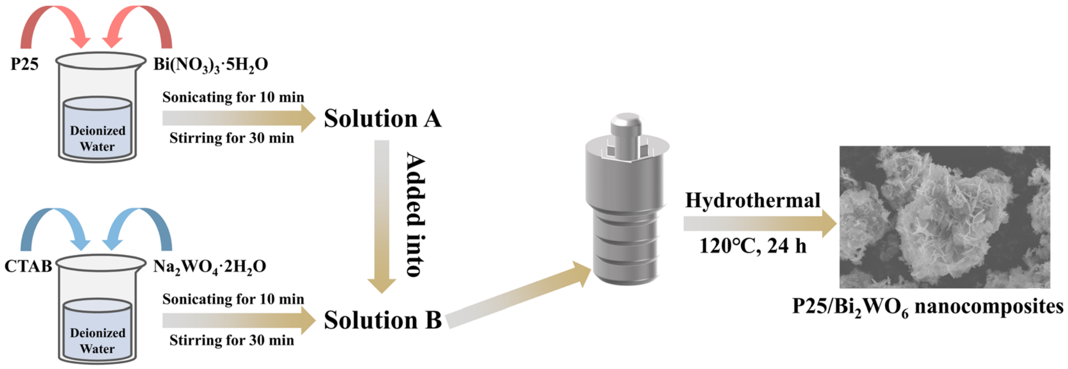

Scheme 1 Schematic illustration of the preparation process of the P25/Bi_2WO_6 composite.

2.3. Characterization

Powder X-ray diffraction (XRD, Rigaku D/MAX 2500 V, Rigaku Corporation, Japan) was used to investigate the crystal phase structure. The wavelength of the copper target was $\lambda = 0.15418$ nm, and the working current and accelerating voltage were 150 mA and 40 kV, respectively. The appearance and micro shape of the catalysts were analyzed by scanning electron microscope (SEM, Sigma 300, Carl Zeiss, Germany) and scanning transmission electron microscope (TEM, Tecnai F20, FEI, USA), respectively. The accelerating voltages of SEM and TEM were 20 kV and 200 kV, respectively. The sample's elemental distribution was detected using energy dispersive spectroscopy (EDS) of Oxford Instrument. The chemical environments of elements on the catalyst's surface were characterized by X-ray photoelectron spectroscopy (XPS, ESCALAB 250XI, Waltham, USA). Before deconvolution, calibration was performed, where all the binding energies were charged and corrected by setting the adventitious carbon signal (C 1s) to 284.8 eV. Raman spectrometer (inVia Reflex 1500080S, Nottingham, UK) was employed to characterize the surface structure of the catalysts. Fourier Transform infrared spectroscopy (FT-IR) spectra were carried out with a Fourier transform infrared spectrometer (FT-IR, Nicolet iS50, Thermo Fisher Scientific, USA). UV-vis diffuse reflectance spectra (DRS, UV-3600Plus, SHIMADZU, Japan) were obtained to investigate the light-harvesting ability of the catalysts. Photoluminescence spectra (PL, FL3C-111 TCSPC, HORIBA, Japan) was obtained to study carriers' separation of samples.

2.4. Photoelectrochemical measurement

The photocatalyst samples' photoelectrochemical (PEC) properties were evaluated using an electrochemical workstation (CHI660D, Chenhua Instrument, China) with a three-electrode system. The samples coated on pure fluorine-doped tin oxide (FTO) glasses acted as working electrodes, while Pt and Ag/AgCl electrodes acted as counter and reference electrodes, respectively, with 0.5 M Na_2SO_4 as the electrolyte solution. A full spectrum Xe lamp (300 W, PLS-SXE300, Perfect light, China) was adopted as the light source.

2.5. Photocatalytic CO_2 reduction experiments

The photocatalytic CO_2 reduction reaction (CO_2RR) was realized in a 100 mL confined device equipped with circulating condensate water and a 300 W Xe lamp (UV light spectrum range of 320–780 nm). In a typical process, 20 mg photocatalyst was ultrasonically dispersed into ethanol and dispensed onto a 30 mm × 30 mm flat quartz plate. After thoroughly drying the catalyst, the flat quartz plate was placed into the reactor. Then, 40 mL 0.1 M $NaHCO_3$ aqueous solution was injected to react. Before irradiation, the reaction mixture was purged with bubbling CO_2 for 40 min in the dark to ensure adsorption–desorption equilibrium was attained on the photocatalyst surface. The reactor's temperature was controlled at 25 °C by cooling water circulation. Then the reactor was continuously irradiated with UV-vis light using a 300 W Xe lamp. After an hour of reaction, the gaseous products were analyzed by a gas chromatograph (GC-2014C, SHIMADZU, Japan) equipped with a flame ionization detector (FID) and a thermal conductivity detector (TCD).

2.6. *In situ* diffuse reflectance infrared Fourier transform spectra (DRIFTS) measurement

In situ diffuse reflectance infrared Fourier transform spectra (DRIFTS) were recorded on a Fourier transform infrared spectrometer (FT-IR, Nicolet iS50, Thermo Fisher Scientific, USA). The spectra in absorbance units were acquired with a resolution of 4 cm^{-1} using 32 scans. Firstly, samples were purged with Ar for an hour, and then a mixture of CO_2 and water vapor was taken into the chamber at 5 mL min^{-1} for 20 min. After that, samples were under illumination (300 W Xe lamp) for 40 min. The spectra were collected every 10 min.

3 Results and discussion

3.1. Structural characterization

The crystalline phases of P25, BWO, and P25/BWO nanocomposites with different contents were analyzed by XRD. As shown in Fig. 1a, the diffraction peaks located at 28.3°, 32.8°, 47.3°, 56.1°, and 58.4° belonged to the (131), (200), (202), (133), and (262) crystalline planes of BWO (JCPDS no. 39-0256), respectively.[38] The diffraction peaks located at 25.3°, 37.8°, 48.0°, 55.0°, and 62.7° assigned to the (101), (004), (200), (211), and (204) crystal planes of anatase TiO_2 (JCPDS no. 21-1272), respectively. The diffraction peaks located at 27.4°, 36.0°, and 41.2° corresponded to the (110), (101), and (111) crystal planes of rutile TiO_2 (JCPDS no. 21-1276), respectively.[39] The peaks of pure P25 and BWO were sharp and had high intensity, indicating that the prepared samples had good crystallinity. Only the diffraction peaks of P25 and BWO appeared in the X-ray diffractograms of all four nanocomposites. The larger the percentage of P25 content, the stronger the intensity of the characteristic peaks of P25 in the nanocomposites. The results indicated that the combination of P25 and BWO had high purity and crystallinity.

FT-IR investigated the specific functional groups of all samples. As shown in Fig. 1b, in the FT-IR spectra of BWO, the peaks at 3447 and 1636 cm^{-1} were caused by O–H vibrations. In addition, the peaks at 1389, 728, and 576 cm^{-1} corresponded to W–O–W stretching, Bi–O stretching, and W–O stretching, respectively.[40] In the FT-IR spectra of P25, the stretching vibrational band from 850 to 433 cm^{-1} belonged to the Ti–O–Ti bond of P25.[21] The four P25/BWO nanocomposites with different contents had both the characteristic absorption peaks of P25 and BWO. Meanwhile, their FT-IR spectra were more similar to that of BWO, which may be because BWO was the main component in the nanocomposites. The above experimental results can prove the successful synthesis of P25/BWO nanocomposites.

Raman spectra were used to investigate the structure of the samples further. Fig. 1c shows the Raman spectra of P25, BWO, and P25/BWO nanocomposites with different contents of

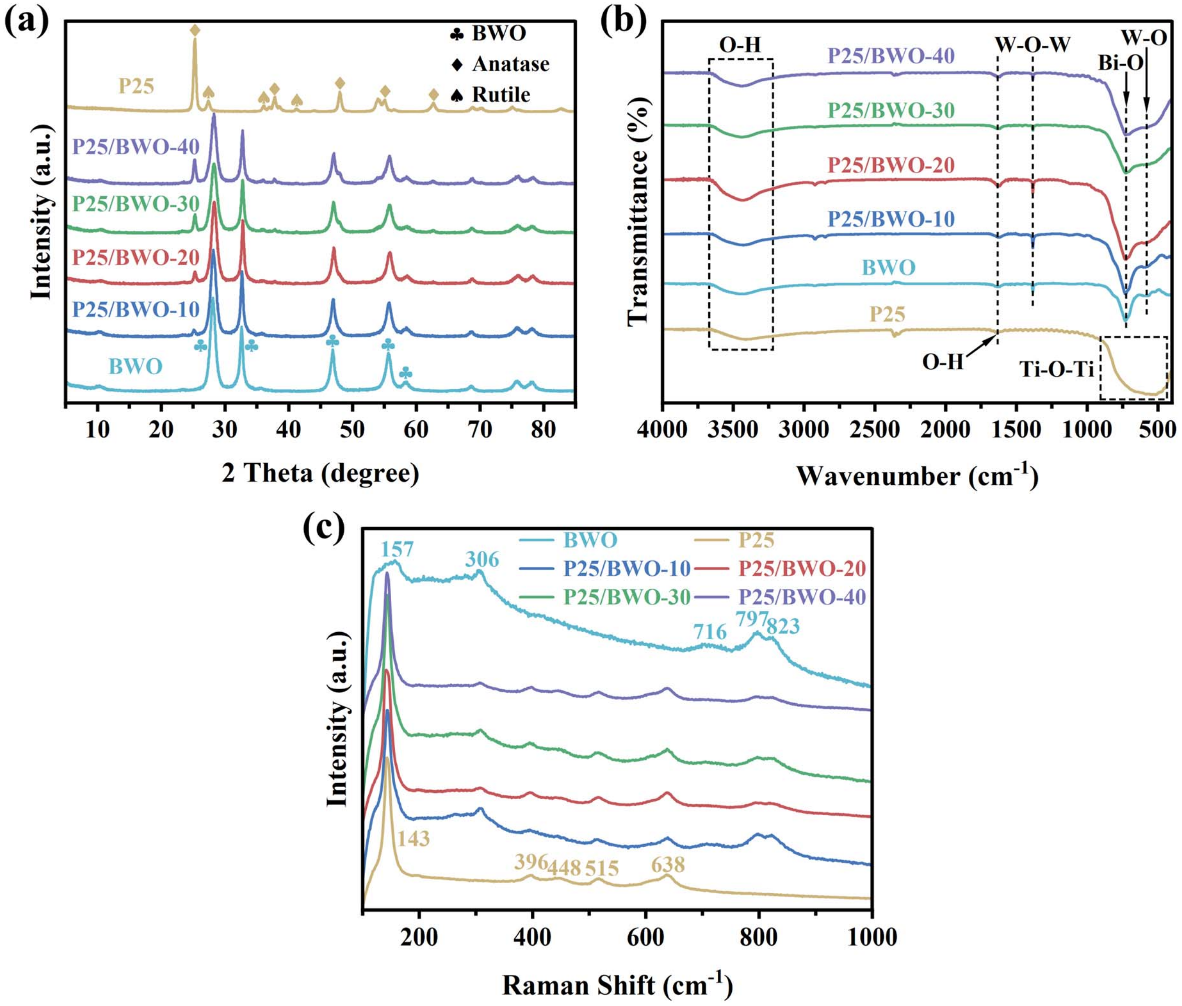

Fig. 1 (a) XRD patterns, (b) FT-IR spectra, and (c) Raman spectra of the as-prepared samples.

wavenumber in the range of 100 to 1000 cm^{-1}. Generally, the typical characteristic peaks of Raman spectra of BWO were located at 157, 306, 716, 797, and 823 cm^{-1}. Among them, the peak at 157 cm^{-1} was attributed to the external vibration of WO_6^{6-}.[41] The vibrational peaks in the range of 600 to 1000 cm^{-1} were attributed to the vibrational stretching mode of the W–O bond. In contrast, the vibrational peaks near 306 cm^{-1} were mainly attributed to the vibrational stretching mode between Bi^{3+} and WO_6^{6-}.[42] The typical characteristic peaks of Raman spectra of anatase TiO_2 were located at 143, 396, 515, and 638 cm^{-1}, and rutile TiO_2 was located at 448 cm^{-1}. The O–Ti–O variable angle vibration peak with the highest intensity was 143 cm^{-1}. In the Raman spectra of the four P25/BWO nanocomposites with different contents, only the typical characteristic peaks of P25 and BWO appeared. The results indicated that there was a strong interaction between P25 and BWO.

3.2. Morphological characterization

SEM and TEM analyzed the morphology and microstructure of the samples. As shown in Fig. 2a–d, pure P25 was a nanoparticle with agglomerated morphology, and BWO was a nanosheet structure with a hierarchical structure. The formation of this hierarchical structure may be due to the anisotropy and self-assembly of BWO nanosheets. For the P25/BWO-20 heterojunction, many P25 nanoparticles can be uniformly distributed in the BWO nanosheets (Fig. 2e and f). From the high-resolution electron microscopy images (Fig. 2j), it can be seen that the two components, P25 and BWO, were in close contact, forming a clear heterojunction interface rather than a simple physical mixing. The lattice spacing of 0.27 nm was assigned to the (020) crystal plane of BWO,[43] and the lattice spacing of 0.352 nm corresponded to the (101) plane of anatase TiO_2.[44] Elemental EDS spectral analysis (Fig. 2k and S1†) revealed the elemental composition and distribution in the P25/BWO-20 heterojunction, and the elemental profiles of Bi, W, Ti, and O were uniformly distributed, indicating that the P25 nanoparticles are uniformly distributed in the nanocomposites. These results indicated that we successfully constructed P25/BWO heterojunction.

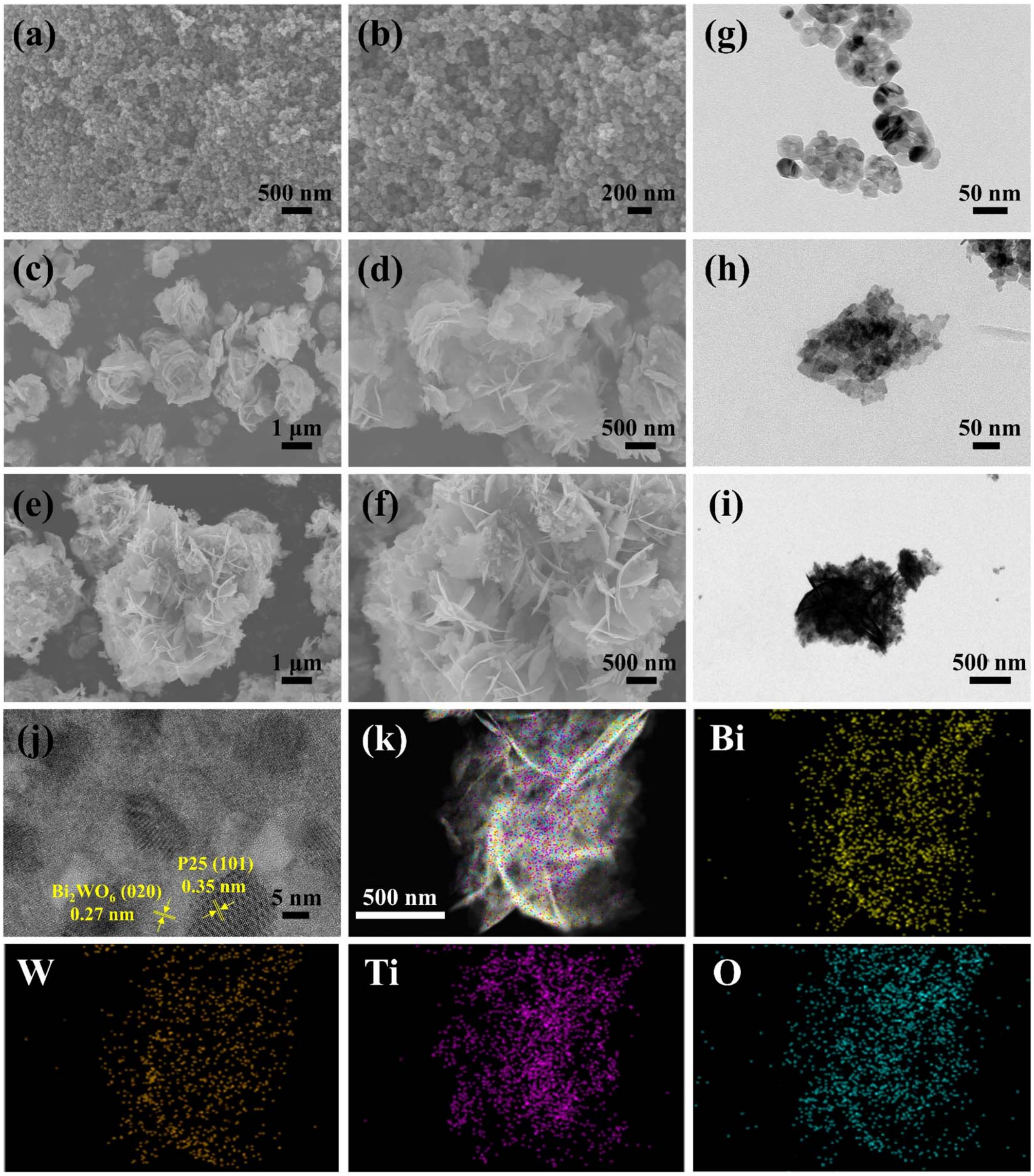

Fig. 2 (a–f) SEM images, and (g–i) TEM images of P25, BWO and P25/BWO-20 heterojunction; (j) HRTEM image, and (k) STEM and the corresponding elemental mapping images of P25/BWO-20 heterojunction.

3.3. Surface and composition analysis

The chemical composition and surface valence states of P25, BWO, and P25/BWO-20 heterojunction were investigated by XPS. Full-spectrum analysis of different samples (Fig. S2†) showed that the P25/BWO-20 heterojunction was mainly composed of four elements, Bi, W, Ti, and O. In order to elucidate the interfacial interaction between P25 and BWO, the high-resolution XPS spectra of different samples of Bi 4f, W 4f, Ti 2p, and O 1s were also investigated. The Bi 4f spectrum of BWO (Fig. 3a) had two peaks at 159.40 and 164.70 eV, which were attributed to Bi $4f_{7/2}$ and Bi $4f_{5/2}$ of the Bi^{3+} ion, respectively. As displayed in Fig. 3b clearly, the peaks at 35.70 and 37.80 eV of the W 4f spectrum corresponded to W $4f_{7/2}$ and W $4f_{5/2}$ of the W^{6+} ion in BWO, respectively.[45] As shown in Fig. 3d, the characteristic peaks with binding energies of 458.45 and 464.25 eV were designated as Ti $2p_{3/2}$ and Ti $2p_{1/2}$, respectively, indicating the presence of Ti^{4+}.[21] Compared to the pristine BWO, the P25/BWO-20 heterojunction's binding energies were negatively shifted by 0.1 and 0.15 eV for Bi 4f and W 4f, respectively. Specifically, the negative shift in binding energy indicates an increase in electron density.[46] Therefore, the migration path of electrons in the composite can be determined by shifting the XPS binding energy. In this case, the negative shifts of the binding energy of Bi 4f and W 4f indicated that BWO acts as an electron acceptor in the P25/BWO-20 heterojunction. In order to balance the electron redistribution in the P25/BWO-20 heterojunction, Ti in P25 will be electron deficient. The latter was confirmed by the positive shift of the Ti 2p

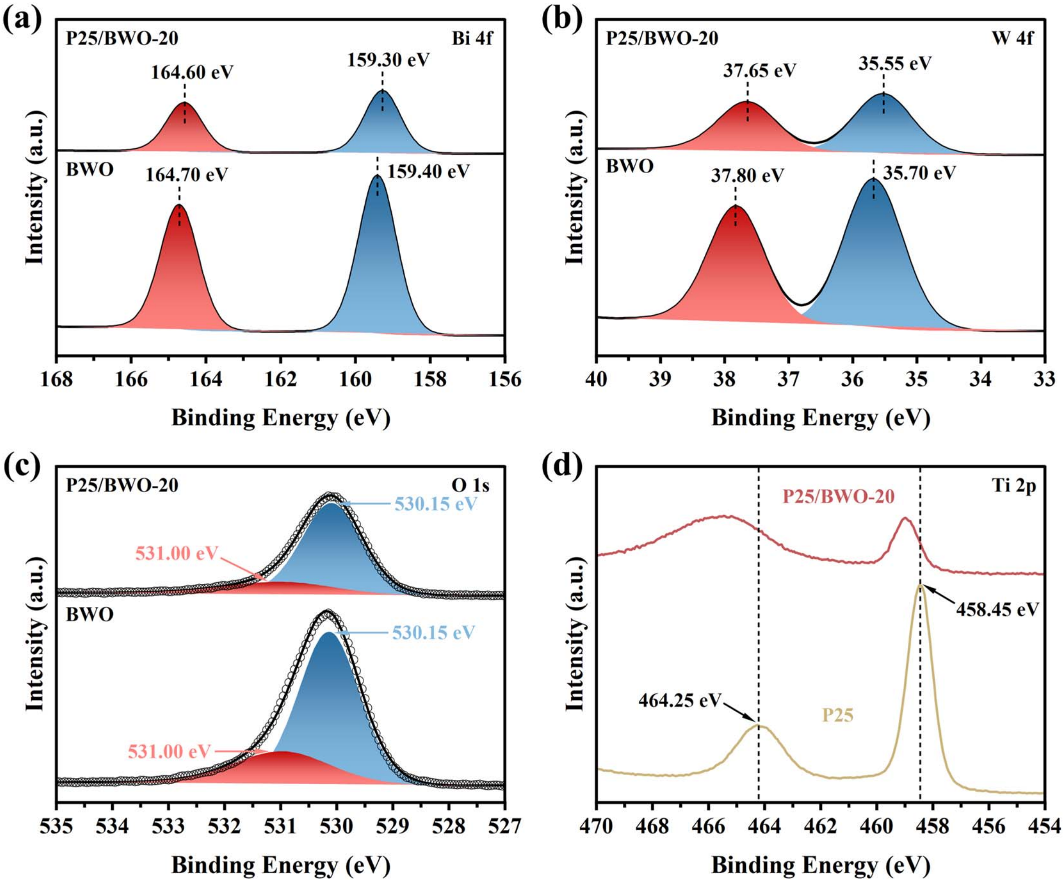

Fig. 3 High-resolution XPS spectra of (a) Bi 4f, (b) W 4f, and (c) O 1s in P25/BWO-20 heterojunction and BWO, and (d) Ti 2p in P25/BWO-20 heterojunction and P25.

binding energy in the P25/BWO-20 heterojunction, which implied a decrease in electron density. In addition, the O 1s spectrum of the P25/BWO-20 heterojunction (Fig. 3c) can be divided into two peaks at 530.15 and 531.00 eV, which were attributed to the lattice oxygen and surface hydroxyl group, respectively.[47,48] By observing the binding energy, the results indicated that the photogenerated electrons migrate from P25 to BWO during photoexcitation, where P25 was the electron donor and BWO was the electron acceptor. The detailed mechanism of the electron transfer pathway in the P25/BWO-20 heterojunction will be further elaborated later.

3.4. Optical properties and energy band structure

The optical absorbance and energy band structure of P25, BWO, and P25/BWO nanocomposites with different contents were investigated by UV-vis DRS. As shown in Fig. 4a and S3,† P25/BWO-20 heterojunction exhibits a feature intermediate between its constituent components, and the absorption edges of P25 and BWO are 414 nm and 449 nm, respectively. Compared with BWO, the absorption edges of the P25/BWO-20 heterojunction showed a slight red-shift and steep curve due to the band gap jump between P25 and BWO. The visible absorption range was extended to 464 nm, indicating that the synthesized nanocomposites had significantly higher light utilization and could absorb solar energy more efficiently and generate electron–hole pairs for photocatalytic CO_2 reduction. Furthermore, based on the Kubelka–Munk equation:[49]

$$\alpha\hbar\nu = k(\hbar\nu - E_g)^{n/2} \tag{1}$$

where α is the absorption coefficient, $\hbar$ is Planck's constant, ν is the incident light frequency, k is a constant, E_g is the bandgap energy, and the value of n for the indirect bandgap semiconductors is 1. Fig. 4b shows the relationship between $(\alpha\hbar\nu)^{1/2}$ and $\hbar\nu$. It was inferred that the band gap widths of P25, BWO, and P25/BWO-20 heterojunction were 3.18, 2.75, and 2.62 eV, respectively. In summary, the enhanced light absorption and narrower forbidden bandwidths were favorable to improve the photocatalytic activity.

Mott–Schottky analysis was performed by impedance-potential testing in a typical three-electrode system to determine the semiconductor type and electronic energy band structure of the sample, where Mott–Schottky diagrams were plotted according to the following equations:[50]

For p-type semiconductors:

$$\frac{1}{C^2} = \frac{2}{e\varepsilon\varepsilon_0 N_A}\left(E_{fb} - E - \frac{K_B T}{e}\right) \tag{2}$$

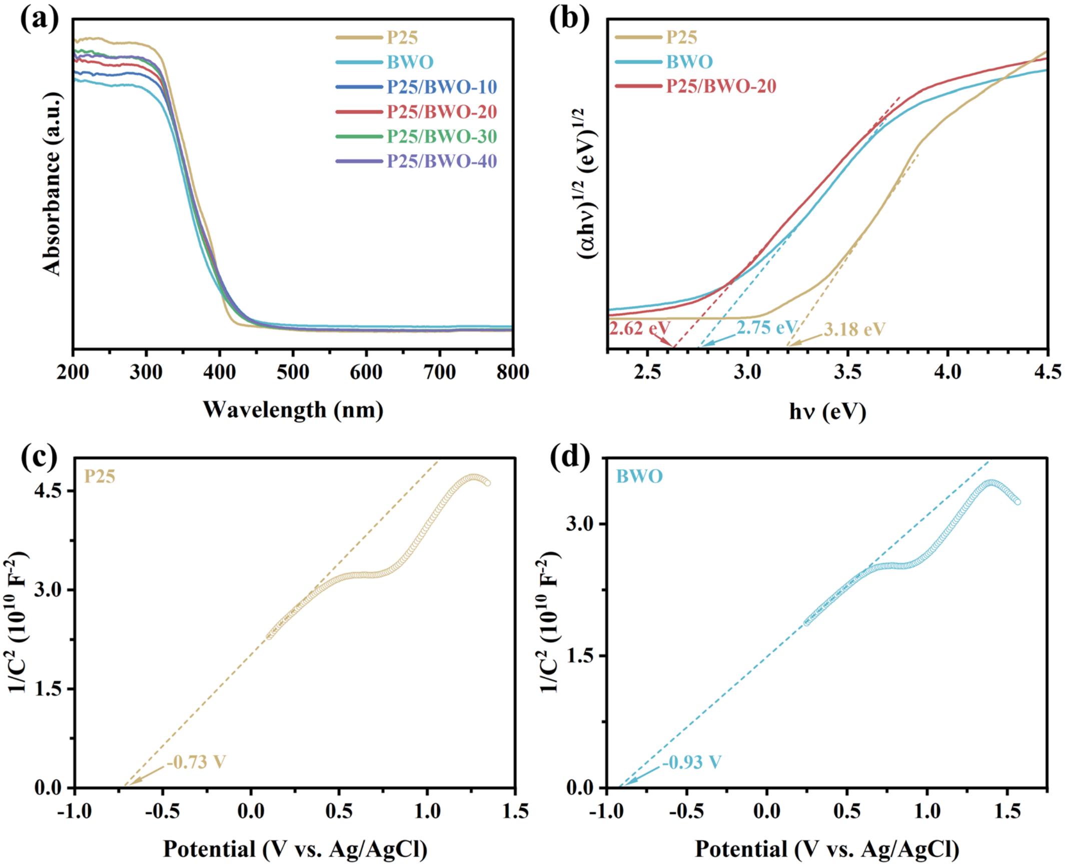

Fig. 4 (a) UV-vis DRS, and (b) Tauc plots of P25, BWO and P25/BWO-20 heterojunction; (c and d) Mott–Schottky plots of P25 and BWO.

For n-type semiconductors:

$$\frac{1}{C^2} = \frac{2}{e\varepsilon\varepsilon_0 N_D}\left(E - E_{fb} - \frac{K_B T}{e}\right) \quad (3)$$

where C is the capacitance of the space charge layer, e is the electronic charge ($e = 1.602 \times 10^{-19}$ C), ε is the dielectric constant of the semiconductor, ε_0 is the permittivity in vacuum ($\varepsilon_0 = 8.8510^{-14}$ F cm^{-1}), N_A and N_D are the numbers of acceptors and donors in p-type and n-type semiconductors, respectively, E is the applied potential, E_{fb} is the flat-band potential, K_B is the Boltzmann's constant, and T is the absolute temperature. Therefore, E_{fb} can be estimated by extrapolating the Mott–Schottky curves to the x-axis (*i.e.*, $1/C^2 = 0$).

As shown in Fig. 4c and d, the slopes of both P25 and BWO are positive, indicating that they were both n-type semiconductors. The experimental potential measured relative to the Ag/AgCl reference electrode can be converted to the standard hydrogen electrode potential by the Nernst equation:[51]

$$E_{fb}(vs.\ \text{NHE}) = E_{fb}(vs.\ \text{Ag/AgCl}) + E^0_{\text{Ag/AgCl}} + 0.059\text{pH} \quad (4)$$

where E_{fb} (*vs.* NHE) is the standard hydrogen electrode potential, E_{fb} (*vs.* Ag/AgCl) is the experimental potential measured against the Ag/AgCl reference electrode and $E^0_{\text{Ag/AgCl}}$ is the standard potential of Ag/AgCl at 298 K (0.1976 V). Considering that the conduction band edge of n-type semiconductors is generally 0.3 V lower than the standard hydrogen electrode potential,[52] the conduction bands of P25 and BWO were calculated to be −0.42 and −0.62 eV, respectively, and the valence bands can be determined by eqn (5):[53]

$$E_{VB} = E_{CB} + E_g \quad (5)$$

The results showed that the valence bands of P25 and BWO were 2.76 and 2.13 eV, respectively.

3.5. Carriers' separation

In addition to the semiconductor energy band structure, the effective electron–hole pair separation is also one of the critical factors affecting photocatalytic efficiency. The samples' charge separation and transfer capability were investigated using transient photocurrent response spectra and AC impedance spectra. Firstly, the transient photocurrent response of the samples was examined by the on–off cycle of simulated solar irradiation. Briefly, photogenerated electrons were transferred to the back contact to generate the photocurrent response.[54,55] Simultaneously, holes migrate to the interface between the photocatalyst and the electrolyte and are then captured by the reduced species in the electrolyte under illumination. Since the electrolyte and electrodes used are the same each time, the instantaneous photocurrent intensity exhibited by the sample reflects the efficiency of photogenerated carrier generation and separation.[56,57] As shown in Fig. 5a, the P25/BWO-20 heterojunction exhibited a higher photocurrent response than pure P25 and BWO, indicating that the P25/BWO-20 heterojunction had better charge separation and transfer efficiency. It was worth mentioning that the photocurrent intensities of the samples were consistent with their results in photocatalytic CO_2 reduction experiments, indicating that separating electron–hole pairs is a decisive factor in photocatalytic performance. In addition, in the absence of light, the photocurrent intensity of the samples was decaying, which can be attributed to the slow discharge of the accumulated charge in the middle layer of the electrodes.[58] The AC impedance spectra can reflect the charge transfer kinetics at the electrode/electrolyte interface. The smaller the arc radius of the curve, the lower the reaction electron transfer resistance and the faster the photogenerated carrier transfer rate, leading to a more superior interfacial charge transfer process.[59,60] As shown in Fig. 5b, the P25/BWO-20 heterojunction had the smallest arc radius, indicating a faster charge transfer rate at the interface. The results of transient photocurrent response and AC impedance spectra indicated that the presence of heterojunction in the P25/BWO nanocomposites facilitates the electron transfer process, which effectively inhibited the recombination of electron–hole pairs and significantly improved the photocatalytic activity of the samples. Steady-state photoluminescence spectra further verified the charge separation and transferred efficiency of the samples after excitation at 308 nm. As shown in Fig. 5c, pure P25 and BWO had strong fluorescence emissions at ∼468 nm, indicating a severe recombination of carriers. However, the fluorescence intensity significantly decreased after forming P25/BWO heterojunction, indicating that the formation of a heterojunction can effectively suppress the recombination of electron–hole pairs and facilitate the photocatalytic CO_2 reduction.[61] Therefore, these results suggested that the construction of heterojunction is an effective strategy to improve photocatalytic activity.

3.6. Photocatalytic activities

The photocatalytic CO_2 reduction reaction (CO_2RR) was carried out in a closed quartz glass reaction apparatus without adding any co-catalysts, photosensitizers, or sacrificial agents, and the photocatalytic reactions of all samples were studied in the gas–solid system under simulated solar irradiation. As shown in Fig. 6a, pure P25, and BWO photocatalytic activities were not high due to poor charge separation and severe charge recombination. Meanwhile, the main products of both P25 and BWO were CO. When the P25 nanoparticles and BWO nanosheets were compounded, the P25/BWO nanocomposites exhibited stronger photocatalytic activity. The maximum yield of CO reached 15.815 μmol g^{-1} h^{-1} on the P25/BWO nanocomposites, which was 4.04 and 2.80 times higher than that of P25 and BWO, respectively, indicating the formation of a heterojunction

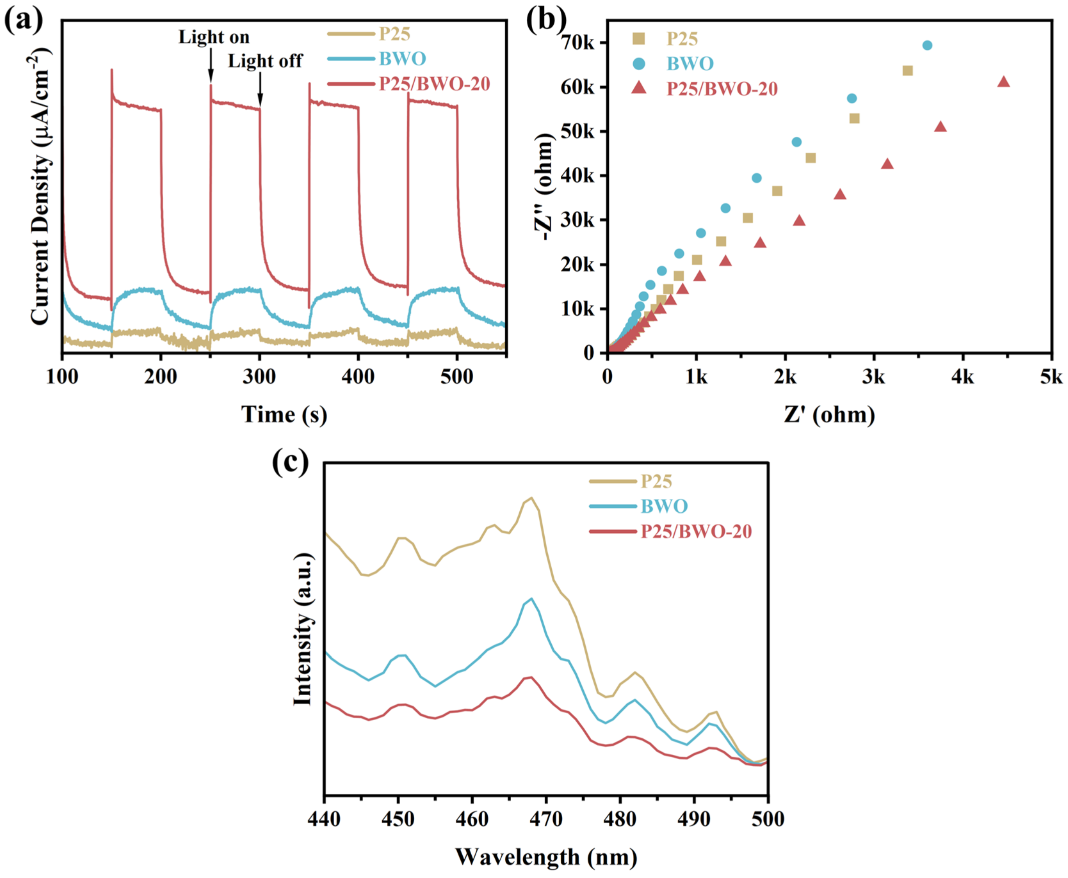

Fig. 5 (a) Transient photocurrent, (b) EIS plots, and (c) PL spectra of P25, BWO and P25/BWO-20 heterojunction.

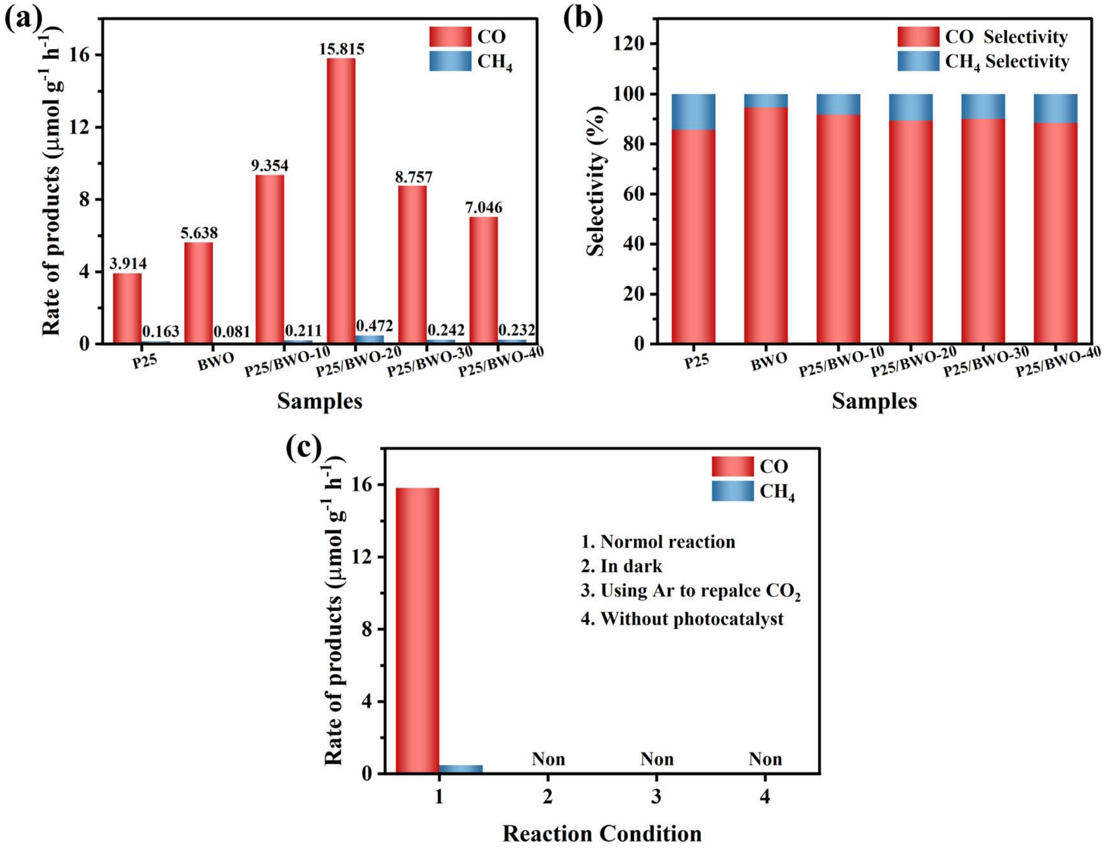

Fig. 6 (a) Photocatalytic activity test, and (b) selectivity of the as-prepared samples; (c) photocatalysis under different conditions performance chart of P25/BWO-20 heterojunction.

between the P25 and BWO interfaces. In addition, the content of P25 in the P25/BWO nanocomposites was optimized, and the results showed that the photocatalytic activity of the samples was enhanced with the increase of P25 content in the nanocomposites, showing a volcanic trend, and the optimal content of P25 in the nanocomposites could be concluded to be 20%. Optimizing the content of P25 can improve the light absorption efficiency of the P25/BWO heterojunction. However, the excessive P25 will block the catalytic active center of the heterojunction and reduce the photocatalytic activity. The product selectivity can observe the effect of the loading of P25 in the nanocomposites on the reduction of CO_2. Based on the number of electrons transferred to produce each reduction product (2e$^-$ for CO and 8e$^-$ for CH_4), the selectivity of CO is defined as follows:[62]

$$S_{\mathrm{CO}} = \frac{2R_{\mathrm{CO}}}{2R_{\mathrm{CO}} + 8R_{\mathrm{CH_4}}} \times 100\% \tag{6}$$

where S_{CO} is the selectivity of CO, R_{CO} and $R_{\mathrm{CH_4}}$ are the yields of CO and CH_4, respectively. Fig. 6b shows the calculated selectivity of CO and CH_4 for all samples. The selectivity of pure P25 and BWO for CO was 85.69% and 94.58%, respectively. For the P25/BWO nanocomposites, the selectivity of CO was ~90%. The results indicated that P25/BWO nanocomposites have a high selectivity for CO, mainly due to the easy desorption of CO and the need for more complex intermediates for CH_4 generation. In addition, a series of control experiments (Fig. 6c) were performed in the absence of light, CO_2, or photocatalyst, where the product yields were negligible, which could indicate that light is the driving force of the CO_2 reduction process and that the carbon source of the product CO was derived from CO_2.

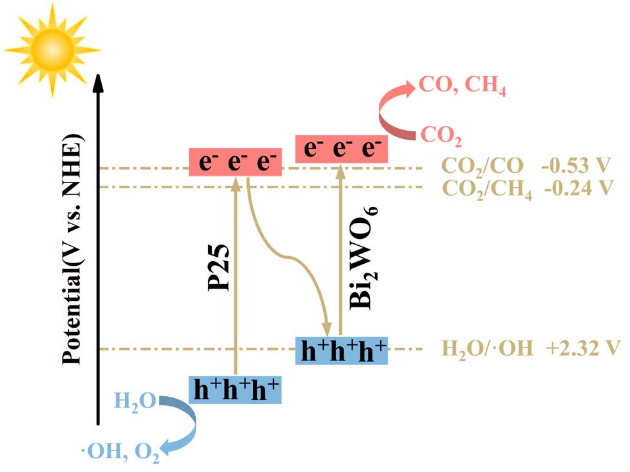

Scheme 2 Proposed mechanism of CO_2 photoreduction due to heterojunction formation within over P25/BWO nanocomposites.

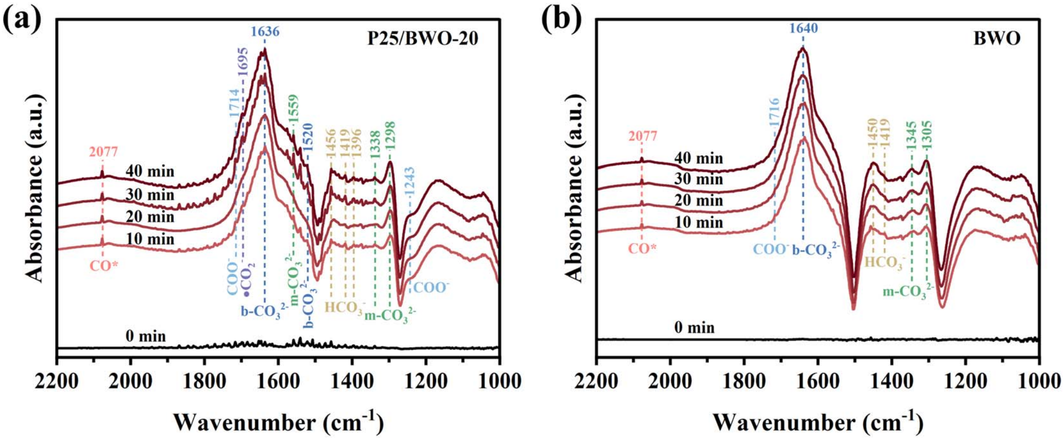

Fig. 7 (a and b) *In situ* DRIFTS spectra of surface adsorbed CO_2 species and photocatalytic CO_2 reduction intermediates of P25/BWO-20 heterojunction and BWO.

3.7. Photocatalytic mechanism of CO_2 reduction

Based on the results above, the charge transfer path at the P25/BWO heterojunction interface may follow the Z-scheme mechanism. As shown in Scheme 2, under simulated solar irradiation, P25 and BWO produce photogenerated electrons and holes in their conduction band (CB) and valence band (VB) positions, respectively, under photoexcitation, where the photogenerated electrons in the CB of P25 will be transferred to the VB of BWO and recombine with the holes produced in the VB. In contrast, the holes in the VB of P25 will react with water (H_2O) to form hydroxyl groups ($\cdot$OH) and protons (H^+). The photogenerated electrons are then retained in the CB of BWO, which can convert CO_2 into CO and CH_4. This Z-scheme charge transfer mechanism enables the P25/BWO nanocomposites to have an efficient charge separation capability, which significantly improves the photocatalytic CO_2 reduction performance of the P25/BWO nanocomposites. It is well known that the different structural characteristics and reaction conditions of catalysts lead to different reaction products. In the photocatalytic CO_2 reduction reaction (CO_2RR), eight electrons ($8e^-$) are required to generate one CH_4 molecule, while only two electrons ($2e^-$) are required to generate one CO molecule. Therefore, it will be more challenging to generate CH_4. Converting CO_2 to CO may be more kinetically advantageous in our photocatalytic reaction system. Therefore, in the present work, the P25/BWO nanocomposites can convert CO_2 into CO with very high selectivity.

In order to explore the process and intermediates of efficient and selective reduction of CO_2 to CO for photocatalysts in more detail, *in situ* diffuse reflectance infrared Fourier transform spectra (DRIFTS) was carried out. Fig. 7a, b and S4† showed the carbon-based groups' dynamic changes on the photocatalysts' surface within 0–40 min of illumination. Several characteristic peaks attributed to bicarbonate (HCO_3^-, 1456, 1419, and 1396 cm^{-1}), monodentate carbonate (m-CO_3^{2-}, 1559, 1338, and 1298 cm^{-1}), bidentate carbonate (b-CO_3^{2-}, 1636 and 1520 cm^{-1}), carboxylate (COO^-, 1714 and 1243 cm^{-1}), and active $\cdot CO_2^-$ intermediates (1695 cm^{-1}) were detected. Hence, the photocatalytic CO_2 reduction can be significantly enhanced due to those important intermediates. In comparison, the signal changes of carbonate and bicarbonate species during reaction processes in the spectra for P25 and BWO are much weaker, indicating a poor ability of CO_2 conversion under the illumination of P25 and BWO. Moreover, the significant peak absorbance of CO* (2077 cm^{-1}) supports the formation of CO during photocatalytic CO_2 reduction.[7,63–65]

4 Conclusions

In summary, we prepared P25/BWO nanocomposites by a one-step *in situ* hydrothermal method for efficient photocatalytic CO_2 reduction. Their respective interlaced energy band structures promote charge separation and inhibit charge recombination. The P25/BWO nanocomposites exhibited strong synergy between the semiconductor components, leading to good activity and selectivity for the photoreduction of CO_2 to CO under simulated solar irradiation. The samples had the highest activity when the content of P25 in the nanocomposites is 20%, when maximization of the heterojunction interface may be achieved. The CO yield of the P25/BWO-20 heterojunction reached 15.815 μmol g^{-1} h^{-1}, which was 4.04 and 2.80 times higher than that of pure P25 and BWO, respectively. In addition, the P25/BWO-20 heterojunction showed a high selectivity of 89.33% for CO, mainly due to the easy desorption of CO and the need for more complex intermediates for CH_4 generation. This work presents an effective strategy to facilitate charge separation by constructing Z-scheme heterojunction. This strategy opens up new opportunities for designing and developing other novel Bi_2WO_6-based photocatalysts.

Ethical approval

The experimental protocols were not involved by any animals or human care.

Data availability

The datasets used and/or analyzed during the current study are available from the corresponding author on reasonable request.

Author contributions

D. Liu: Investigation, Data Curation, writing – original draft; M. Zeng: validation, formal analysis, writing – review & editing; Z. Li: methodology; Z. Zhu: resources; Y. Chen: data curation; K. Thummavichai: supervision; O. Ola: investigation, formal analysis; N. Wang: project administration; Y. Zhu: conceptualization, funding acquisition.

Conflicts of interest

The authors have no conflicts of interest to declare.

Acknowledgements

This work was supported by National Natural Science Foundation (51972068), Natural Science Foundation of Guangxi Province (2021GXNSFBA076003), Guangxi Key Laboratory of Manufacturing Systems and Advanced Manufacturing Technology (20-065-40S007), the Interdisciplinary Scientific Research Foundation of Guangxi University (Grant No. 2022JCA002).

References

1 S. Cestellos-Blanco, H. Zhang, J. M. Kim, Y.-x. Shen and P. Yang, Photosynthetic semiconductor biohybrids for solar-driven biocatalysis, *Nat. Catal.*, 2020, **3**, 245–255.
2 X. Wang, J. He, J. Li, G. Lu, F. Dong, T. Majima and M. Zhu, Immobilizing perovskite $CsPbBr_3$ nanocrystals on Black phosphorus nanosheets for boosting charge separation and photocatalytic CO_2 reduction, *Appl. Catal., B*, 2020, **277**, 119230.
3 Y. Yamazaki, M. Miyaji and O. Ishitani, Utilization of Low-Concentration CO_2 with Molecular Catalysts Assisted by CO_2-Capturing Ability of Catalysts, Additives, or Reaction Media, *J. Am. Chem. Soc.*, 2022, **144**(15), 6640–6660.
4 S. Yoshino, T. Takayama, Y. Yamaguchi, A. Iwase and A. Kudo, CO_2 Reduction Using Water as an Electron Donor over Heterogeneous Photocatalysts Aiming at Artificial Photosynthesis, *Acc. Chem. Res.*, 2022, **55**(7), 966–977.
5 W. Zhang, A. R. Mohamed and W.-J. Ong, Z-Scheme Photocatalytic Systems for Carbon Dioxide Reduction: Where Are We Now?, *Angew. Chem., Int. Ed.*, 2020, **59**(51), 22894–22915.
6 P. Zhou, Y. Chao, F. Lv, J. Lai, K. Wang and S. Guo, Designing noble metal single-atom-loaded two-dimension photocatalyst for N_2 and CO_2 reduction via anion vacancy engineering, *Sci. Bull.*, 2020, **65**(9), 720–725.
7 X.-X. Li, L. Zhang, L. Yuan, T. Wang, L.-Z. Dong, K. Huang, J. Liu and Y.-Q. Lan, Constructing crystalline redox catalyst to achieve efficient CO_2 photoreduction reaction in water vapor, *Chem. Eng. J.*, 2022, **442**, 136157.
8 T. Inoue, A. Fujishima, S. Konishi and K. Honda, Photoelectrocatalytic reduction of carbon dioxide in aqueous suspensions of semiconductor powders, *Nature*, 1979, **277**, 637–638.
9 X. Cui, J. Wang, B. Liu, S. Ling, R. Long and Y. Xiong, Turning Au Nanoclusters Catalytically Active for Visible-Light-Driven CO_2 Reduction through Bridging Ligands, *J. Am. Chem. Soc.*, 2018, **140**(48), 16514–16520.
10 F. Zhang, Y.-H. Li, M.-Y. Qi, Z.-R. Tang and Y.-J. Xu, Boosting the activity and stability of Ag-Cu_2O/ZnO nanorods for photocatalytic CO_2 reduction, *Appl. Catal., B*, 2020, **268**, 118380.
11 J. Hao, B. Qi, J. Wei, D. Li and F. Zeng, A Z-scheme Cu_2O/WO_3 heterojunction for production of renewable hydrocarbon fuel from carbon dioxide, *Fuel*, 2021, **287**, 119439.
12 C. B. Hiragond, J. Lee, H. Kim, J.-W. Jung, C.-H. Cho and S.-I. In, A novel N-doped graphene oxide enfolded reduced titania for highly stable and selective gas-phase photocatalytic CO_2 reduction into CH_4: an in-depth study on the interfacial charge transfer mechanism, *Chem. Eng. J.*, 2021, **416**, 127978.
13 N. Lin, Y. Lin, X. Qian, X. Wang and W. Su, Construction of a 2D/2D $WO_3/LaTiO_2N$ Direct Z-Scheme Photocatalyst for Enhanced CO_2 Reduction Performance Under Visible Light, *ACS Sustainable Chem. Eng.*, 2021, **9**(40), 13686–13694.
14 L. O. Paulista, J. Albero, R. J. E. Martins, R. A. R. Boaventura, V. J. P. Vilar, T. F. C. V. Silva and H. García, Turning Carbon Dioxide and Ethane into Ethanol by Solar-Driven Heterogeneous Photocatalysis over RuO_2- and NiO-co-Doped $SrTiO_3$, *Catalysts*, 2021, **11**(4), 461.
15 S. Gong, F. Rao, W. Zhang, Q.-U. Hassan, Z. Liu, J. Gao, J. Lu, M. Hojamberdiev and G. Zhu, Au nanoparticles loaded on hollow BiOCl microstructures boosting CO_2 photoreduction, *Chin. Chem. Lett.*, 2022, **33**(9), 4385–4388.
16 M. K. Hussien, A. Sabbah, M. Qorbani, M. H. Elsayed, P. Raghunath, T.-Y. Lin, S. Quadir, H.-Y. Wang, H.-L. Wu, D.-L. M. Tzou, M.-C. Lin, P.-W. Chung, H.-H. Chou, L.-C. Chen and K.-H. Chen, Metal-free four-in-one modification of g-C_3N_4 for superior photocatalytic CO_2 reduction and H_2 evolution, *Chem. Eng. J.*, 2022, **430**, 132853.
17 S. Cao, B. Shen, T. Tong, J. Fu and J. Yu, 2D/2D Heterojunction of Ultrathin MXene/Bi_2WO_6 Nanosheets for Improved Photocatalytic CO_2 Reduction, *Adv. Funct. Mater.*, 2018, **28**(21), 1800136.
18 C. Gao, J. Wang, H. Xu and Y. Xiong, Coordination chemistry in the design of heterogeneous photocatalysts, *Chem. Soc. Rev.*, 2017, **46**(10), 2799–2823.
19 S. Wageh, A. A. Al-Ghamdi, R. Jafer, X. Li and P. Zhang, A new heterojunction in photocatalysis: S-scheme heterojunction, *Chin. J. Catal.*, 2021, **42**(5), 667–669.
20 C.-W. Huang, C.-H. Liao, J. C. S. Wu, Y.-C. Liu, C.-L. Chang, C.-H. Wu, M. Anpo, M. Matsuoka and M. Takeuchi, Hydrogen generation from photocatalytic water splitting over TiO_2 thin film prepared by electron beam-induced

deposition, *Int. J. Hydrogen Energy*, 2010, **35**(21), 12005–12010.

21 Z. Xiong, Y. Zhao, J. Zhang and C. Zheng, Efficient photocatalytic reduction of CO_2 into liquid products over cerium doped titania nanoparticles synthesized by a sol-gel auto-ignited method, *Fuel Process. Technol.*, 2015, **135**, 6–13.

22 L. Wang, Z. Zhang, Q. Han, Y. Liu, J. Zhong, J. Chen, J. Huang, H. She and Q. Wang, Preparation of CdS-P25/ZIF-67 composite material and its photocatalytic CO_2 reduction performance, *Appl. Surf. Sci.*, 2022, **584**, 152645.

23 T. Wang, Y. Zhang, J. Pan, B. Li, L. Wu and B. Jiang, Hydrothermal reduction of commercial P25 photocatalysts to expand their visible-light response and enhance their performance for photodegrading phenol in high-salinity wastewater, *Appl. Surf. Sci.*, 2019, **480**, 896–904.

24 K. Nakata and A. Fujishima, TiO_2 photocatalysis: Design and applications, *J. Photochem. Photobiol., C*, 2012, **13**(3), 169–189.

25 M. Pelaez, N. T. Nolan, S. C. Pillai, M. K. Seery, P. Falaras, A. G. Kontos, P. S. M. Dunlop, J. W. J. Hamilton, J. A. Byrne, K. O'Shea, M. H. Entezari and D. D. Dionysiou, A review on the visible light active titanium dioxide photocatalysts for environmental applications, *Appl. Catal., B*, 2012, **125**, 331–349.

26 J. Low, J. Yu and W. Ho, Graphene-Based Photocatalysts for CO_2 Reduction to Solar Fuel, *J. Phys. Chem. Lett.*, 2015, **6**(21), 4244–4251.

27 P. Kar, S. Farsinezhad, N. Mahdi, Y. Zhang, U. Obuekwe, H. Sharma, J. Shen, N. Semagina and K. Shankar, Enhanced CH_4 yield by photocatalytic CO_2 reduction using TiO_2 nanotube arrays grafted with Au, Ru, and ZnPd nanoparticles, *Nano Res.*, 2016, **9**(11), 3478–3493.

28 S. Kawamura, H. Zhang, M. Tamba, T. Kojima, M. Miyano, Y. Yoshida, M. Yoshiba and Y. Izumi, Efficient volcano-type dependence of photocatalytic CO_2 conversion into methane using hydrogen at reaction pressures up to 0.80 MPa, *J. Catal.*, 2017, **345**, 39–52.

29 K. Li, C. Teng, S. Wang and Q. Min, Recent Advances in TiO_2-Based Heterojunctions for Photocatalytic CO_2 Reduction With Water Oxidation: A Review, *Front. Chem.*, 2021, **9**, 637501.

30 N. Kim, R.-N. Vannier and C. P. Grey, Detecting Different Oxygen-Ion Jump Pathways in Bi_2WO_6 with 1- and 2-Dimensional 17O MAS NMR Spectroscopy, *Chem. Mater.*, 2005, **17**(8), 1952–1958.

31 N. Zhang, R. Ciriminna, M. Pagliaro and Y.-J. Xu, Nanochemistry-derived Bi_2WO_6 nanostructures: towards production of sustainable chemicals and fuels induced by visible light, *Chem. Soc. Rev.*, 2014, **43**(15), 5276–5287.

32 M. Sun, X. Dong, B. Lei, J. Li, P. Chen, Y. Zhang and F. Dong, Graphene oxide mediated co-generation of C-doping and oxygen defects in Bi_2WO_6 nanosheets: a combined DRIFTS and DFT investigation, *Nanoscale*, 2019, **11**(43), 20562–20570.

33 M. Li, L. Zhang, X. Fan, Y. Zhou, M. Wu and J. Shi, Highly selective CO_2 photoreduction to CO over g-C_3N_4/Bi_2WO_6 composites under visible light, *J. Mater. Chem. A*, 2015, **3**(9), 5189–5196.

34 J. Hu, D. Chen, Z. Mo, N. Li, Q. Xu, H. Li, J. He, H. Xu and J. Lu, Z-Scheme 2D/2D Heterojunction of Black Phosphorus/Monolayer Bi_2WO_6 Nanosheets with Enhanced Photocatalytic Activities, *Angew. Chem., Int. Ed.*, 2019, **58**(7), 2073–2077.

35 H. Salari, Facile template-free synthesis of 3D flower-like Bi_2WO_6/MoO_3 nanocomposites with ultra-thin sheets and their associated photocatalytic properties under visible light irradiation, *J. Photochem. Photobiol., A*, 2019, **385**, 112069.

36 Y. Zhang, C. Xu, F. Wan, D. Zhou, L. Yang, H. Gu and J. Xiong, Synthesis of flower-like $Bi_2Sn_2O_7$/Bi_2WO_6 hierarchical composites with enhanced visible light photocatalytic performance, *J. Alloys Compd.*, 2019, **788**, 1154–1161.

37 J. Tian, L. Wei, Z. Ren, J. Lu and J. Ma, The facile fabrication of Z-scheme Bi_2WO_6-P25 heterojunction with enhanced photodegradation of antibiotics under visible light, *J. Environ. Chem. Eng.*, 2021, **9**(5), 106167.

38 J. Wang, L. Tang, G. Zeng, Y. Deng, Y. Liu, L. Wang, Y. Zhou, Z. Guo, J. Wang and C. Zhang, Atomic scale g-C_3N_4/Bi_2WO_6 2D/2D heterojunction with enhanced photocatalytic degradation of ibuprofen under visible light irradiation, *Appl. Catal., B*, 2017, **209**, 285–294.

39 K. Kalantari, M. Kalbasi, M. Sohrabi and S. J. Royaee, Enhancing the photocatalytic oxidation of dibenzothiophene using visible light responsive Fe and N co-doped TiO_2 nanoparticles, *Ceram. Int.*, 2017, **43**(1), 973–981.

40 S. Xiong, S. Bao, W. Wang, J. Hao, Y. Mao, P. Liu, Y. Huang, Z. Duan, Y. Lv and D. Ouyang, Surface oxygen vacancy and graphene quantum dots co-modified Bi_2WO_6 toward highly efficient photocatalytic reduction of CO_2, *Appl. Catal., B*, 2022, **305**, 121026.

41 J. Cheng, S. Shi, T. Tang, S. Tian, W. Yang and D. Zeng, Controllable topological transformation from BiOCl hierarchical microspheres to Bi_2WO_6 superstructures in the Bi–W–Cl–O system, *J. Alloys Compd.*, 2015, **643**, 159–166.

42 M. Mączka, L. Macalik, K. Hermanowicz, L. Kępiński and P. Tomaszewski, Phonon properties of nanosized bismuth layered ferroelectric material-Bi_2WO_6, *J. Raman Spectrosc.*, 2010, **41**(9), 1059–1066.

43 Y. Zhou, Z. Tian, Z. Zhao, Q. Liu, J. Kou, X. Chen, J. Gao, S. Yan and Z. Zou, High-yield synthesis of ultrathin and uniform Bi_2WO_6 square nanoplates benefitting from photocatalytic reduction of CO_2 into renewable hydrocarbon fuel under visible light, *ACS Appl. Mater. Interfaces*, 2011, **3**(9), 3594–3601.

44 S. Liu, S. Wang, C. Lei, R. Li, S. Feng and Q. Jin, Study of the efficiency of g-C_3N_4-loaded P25 for photocatalytic degradation of malachite green in aqueous and Pickering emulsion systems, *J. Mater. Sci.: Mater. Electron.*, 2022, **33**, 5846–5858.

45 G. Zhang, Z. Hu, M. Sun, Y. Liu, L. Liu, H. Liu, C.-P. Huang, J. Qu and J. Li, Formation of Bi_2WO_6 Bipyramids with

Vacancy Pairs for Enhanced Solar-Driven Photoactivity, *Adv. Funct. Mater.*, 2015, **25**(24), 3726–3734.

46 J. Low, C. Jiang, B. Cheng, S. Wageh, A. A. Al-Ghamdi and J. Yu, A Review of Direct Z-Scheme Photocatalysts, *Small Methods*, 2017, **1**(5), 1700080.

47 Y. Zhou, Y. Zhang, M. Lin, J. Long, Z. Zhang, H. Lin, J. C.-S. Wu and X. Wang, Monolayered Bi_2WO_6 nanosheets mimicking heterojunction interface with open surfaces for photocatalysis, *Nat. Commun.*, 2015, **6**, 8340.

48 H. Huang, R. Cao, S. Yu, K. Xu, W. Hao, Y. Wang, F. Dong, T. Zhang and Y. Zhang, Single-unit-cell layer established Bi_2WO_6 3D hierarchical architectures: Efficient adsorption, photocatalysis and dye-sensitized photoelectrochemical performance, *Appl. Catal., B*, 2017, **219**, 526–537.

49 Y. Huang, K. Wang, T. Guo, J. Li, X. Wu and G. Zhang, Construction of 2D/2D Bi_2Se_3/g-C_3N_4 nanocomposite with High interfacial charge separation and photo-heat conversion efficiency for selective photocatalytic CO_2 reduction, *Appl. Catal., B*, 2020, **277**, 119232.

50 S. Bai, J. Jiang, Q. Zhang and Y. Xiong, Steering charge kinetics in photocatalysis: intersection of materials syntheses, characterization techniques and theoretical simulations, *Chem. Soc. Rev.*, 2015, **44**(10), 2893–2939.

51 W. Yin, L. Bai, Y. Zhu, S. Zhong, L. Zhao, Z. Li and S. Bai, Embedding Metal in the Interface of a p–n Heterojunction with a Stack Design for Superior Z-Scheme Photocatalytic Hydrogen Evolution, *ACS Appl. Mater. Interfaces*, 2016, **8**(35), 23133–23142.

52 L. Xiao, R. Lin, J. Wang, C. Cui, J. Wang and Z. Li, A novel hollow-hierarchical structured Bi_2WO_6 with enhanced photocatalytic activity for CO_2 photoreduction, *J. Colloid Interface Sci.*, 2018, **523**, 151–158.

53 J. Sheng, Y. He, J. Li, C. Yuan, H. Huang, S. Wang, Y. Sun, Z. Wang and F. Dong, Identification of Halogen-Associated Active Sites on Bismuth-Based Perovskite Quantum Dots for Efficient and Selective CO_2-to-CO Photoreduction, *ACS Nano*, 2020, **14**(10), 13103–13114.

54 S. Wang and X. Wang, Photocatalytic CO_2 reduction by CdS promoted with a zeolitic imidazolate framework, *Appl. Catal., B*, 2015, **162**, 494–500.

55 J. Peng, J. Xu, Z. Wang, Z. Ding and S. Wang, Developing an efficient $NiCo_2S_4$ cocatalyst for improving the visible light H_2 evolution performance of CdS nanoparticles, *Phys. Chem. Chem. Phys.*, 2017, **19**(38), 25919–25926.

56 W. P. C. Lee, X. Y. Kong, L.-L. Tan, M. M. Gui, S. Sumathi and S.-P. Chai, Molybdenum disulfide quantum dots decorated bismuth sulfide as a superior noble-metal-free photocatalyst for hydrogen evolution through harnessing a broad solar spectrum, *Appl. Catal., B*, 2018, **232**, 117–123.

57 S. Wang, B. Y. Guan and X. W. D. Lou, Construction of $ZnIn_2S_4$-In_2O_3 Hierarchical Tubular Heterostructures for Efficient CO_2 Photoreduction, *J. Am. Chem. Soc.*, 2018, **140**(15), 5037–5040.

58 L. Yuan, B. Weng, J. C. Colmenares, Y. Sun and Y.-J. Xu, Multichannel Charge Transfer and Mechanistic Insight in Metal Decorated 2D-2D Bi_2WO_6-TiO2 Cascade with Enhanced Photocatalytic Performance, *Small*, 2017, **13**(48), 1702253.

59 B. Shao, Z. Liu, G. Zeng, Z. Wu, Y. Liu, M. Cheng, M. Chen, Y. Liu, W. Zhang and H. Feng, Nitrogen-Doped Hollow Mesoporous Carbon Spheres Modified g-C_3N_4/Bi_2O_3 Direct Dual Semiconductor Photocatalytic System with Enhanced Antibiotics Degradation under Visible Light, *ACS Sustainable Chem. Eng.*, 2018, **6**(12), 16424–16436.

60 M. Zhou, S. Wang, P. Yang, C. Huang and X. Wang, Boron Carbon Nitride Semiconductors Decorated with CdS Nanoparticles for Photocatalytic Reduction of CO_2, *ACS Catal.*, 2018, **8**(6), 4928–4936.

61 Z. Wei, J. Liu, W. Fang, M. Xu, Z. Qin, Z. Jiang and W. Shangguan, Photocatalytic hydrogen evolution with simultaneous antibiotic wastewater degradation via the visible-light-responsive bismuth spheres-g-C_3N_4 nanohybrid: waste to energy insight, *Chem. Eng. J.*, 2019, **358**, 944–954.

62 J. Fu, K. Jiang, X. Qiu, J. Yu and M. Liu, Product selectivity of photocatalytic CO_2 reduction reactions, *Mater. Today*, 2020, **32**, 222–243.

63 X. Jin, J. Cao, H. Wang, C. Lv, H. Xie, F. Su, X. Li, R. Sun, S. Shi, M. Dang and L. Ye, Realizing improved CO_2 photoreduction in Z-scheme $Bi_4O_5Br_2$/AgBr heterostructure, *Appl. Surf. Sci.*, 2022, **598**, 153758.

64 J. Xu, Y. Chen, M. Chen, J. Wang and L. Wang, In situ growth strategy synthesis of single-atom nickel/sulfur co-doped g-C_3N_4 for efficient photocatalytic tetracycline degradation and CO_2 reduction, *Chem. Eng. J.*, 2022, **442**, 136208.

65 X. Zhao, M. Xu, X. Song, W. Zhou, X. Liu, H. Wang and P. Huo, Integration of 3D macroscopic reduced graphene oxide aerogel with DUT-67 for selective CO_2 photoreduction to CO in Gas-Solid reaction, *Chem. Eng. J.*, 2022, **446**, 137034.